Defect Dynamics in Self-Catalyzed III-V Semiconductor Nanowires

James A. Gott[§], Richard Beanland[§]*, H. Aruni Fonseka[§], Jonathan J.P. Peters[§], Yunyan Zhang[†], Huiyun Liu[†] and Ana M. Sanchez[§]*

[§] Department of Physics, University of Warwick, Coventry CV4 7AL, United Kingdom

[†]Department of Electronic and Electrical Engineering, University College London, Torrington Place, London WC1E 7JE, United Kingdom

Abstract:

The droplet consumption step in self-catalyzed III-V semiconductor nanowires can produce material that contains a high density of line defects. Interestingly, these defects are often associated with twin boundaries and have null Burgers vector, i.e. no long-range strain field. Here we analyze their stability by considering the forces that act on them and use in-situ aberration corrected scanning transmission electron microscopy (STEM) to observe their behavior in GaAsP NWs using short annealing cycles. Their movement appears to be consistent with the thermally-activated single- or double-kink mechanisms of dislocation glide, with velocities that do not exceed 1 nm s^{-1}. We find that motion of individual defects depends on their size, position, and surrounding environment and set an upper limit to activation energy around 2eV. The majority of defects (>70%) are removed by our post-growth annealing for several seconds at temperatures in excess of 640 °C, suggesting that in-situ annealing during growth at lower temperatures would significantly improve material quality. The remaining defects do not move at all and are thermodynamically stable in the nanowire.

Keywords: Defects, In-Situ, Nanowires, STEM, TEM

1. Introduction

Compound semiconductor nanowires (NWs) represent a significant advance towards the seamless integration of highly mismatched materials with silicon.[1–9] The ability of NWs to expel line defects with a long-range stain field, i.e. dislocations, overcomes key challenges in device production.[4] The inherent perfection of NWs may allow the production of semiconductor materials and devices without dislocations or cracks, which are currently unobtainable using existing heteroepitaxial layer growth techniques.

In molecular beam epitaxy (MBE), NW growth usually takes place by the vapor-liquid-solid (VLS) mechanism, i.e. by addition of discrete atomic layers at the interface between a catalytic liquid metal droplet and the NW.[10] The production of a functional heterostructure, with different materials and/or dopants, requires changes and interruptions of the molecular beam fluxes. In 'self-catalyzed' III-V NWs the liquid droplet is itself a component of the compound (e.g. Ga, for GaAs NWs) and can be converted into solid material at the end of core growth. Droplet consumption is often essential for any structures that require a change from axial to radial growth, e.g. to subsequently produce core-shell structures.[11,12] An example of a MBE-grown GaAsP NW, in which the Ga droplet has been converted to solid material, is shown in Figure 1a. The material formed by droplet consumption is clearly different from the rest of the NW. We have shown that rough interfaces can be produced as the droplet is consumed and a surprisingly high density of line defects can be found in material grown during this phase.[13,14] The origin of these defects is the instability of the growth front between the crystal NW and the liquid Ga droplet as it is consumed, when the Ga flux is switched off..[11,12] Roughening of the interface can produce multiple islands; the defects observed in this study are produced when twinned islands meet (see supporting information S1). Once these defects form, any subsequent shell growth will copy defects present in the core. These defects will be detrimental to electronic properties and device performance. They can be categorized into two types: defects

with null Burgers vector formed in twin boundaries (the majority) or crystal dislocations that are locked-in by reaction and/or dissociation.[14] Defects with null Burgers vector are almost invisible using conventional (diffraction contrast) transmission electron microscopy and their prevalence in NWs generally is still to be determined. We find them in all self-catalyzed NWs after droplet consumption; they have also been observed in semiconductor NWs by other groups[15] and have been reported previously in copper nanocrystals.[16] The most common null Burgers vector defects are $\Sigma 3$ {112} twin facets with heights constrained to *3n* (111) monolayers (ML), with $n = 1,2,3\ldots$. Twin facets with $n = 1$ are the most common. Since the facet cannot end inside the crystal, but must continue to the NW surface, they can be considered to be null Burgers vector line defects and, for brevity, we refer to them as *3ML defects* in this paper. A pair of 3ML defects is shown in Figure 1b, a false color annular dark field scanning transmission electron microscope (ADF-STEM) image of material in the tip region of a GaAsP NW shown in Figure 1a. The growth direction, [111]B ≡ $[\bar{1}\bar{1}\bar{1}]$ is vertical. The three-monolayer high twin (yellow) is bounded at each end by a $\Sigma 3$ {112} facet while the NW polarity is maintained throughout, i.e. both orange and blue areas have polarity $[\bar{1}\bar{1}\bar{1}]$. As is well-known,[17,13] the two $\Sigma 3$ {112} facets have different core structures in III-V material (Figure 1d). As shown in Figure 1c, the 3ML defect on the left is a "down" step with a pair of under-bonded group V atoms (red), while that on the right is an "up" step with two under-bonded group V atoms (mauve). These 3ML defects thus have deleterious effects on semiconductor properties similar to those of dislocations.[13] This is not surprising, since the termination of twins with height 1ML and 2ML are commonly known as $1/6\langle 112\rangle$ intrinsic and extrinsic partial dislocations respectively. The 3ML defect contains the structural motifs of both; it can, in fact, be considered as a dislocation dipole made up of an intrinsic $1/6\langle 112\rangle$ partial dislocation (green box, Figure 1c) and an extrinsic $1/6\langle \bar{1}\bar{1}\bar{2}\rangle$ dislocation (orange box). It thus bears some similarity to a dissociated $1/2\langle 110\rangle$ crystal dislocation, which also consists of two partial dislocations.

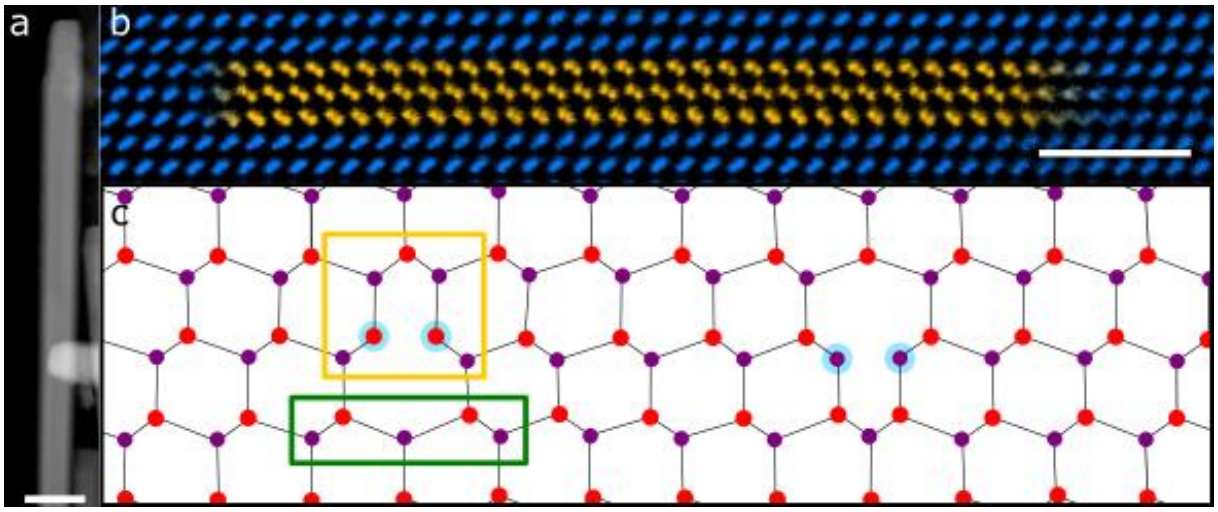

Figure 1. a) An ADF-STEM image of a GaAsP nanowire with a defective tip. b) False color atomic resolution ADF image taken along the $[\bar{1}10]$ direction of the crystal, showing a 3ML high twin (yellow), bounded by Σ3 {112} twin facets at each end. c) Schematic showing the two different core structures of the Σ3 {112} twin facets, with under-bonded atoms corresponding to group V (red) on the left and group III (mauve)on the right. A 3ML defect can also be considered to be a dislocation dipole comprised of a pair of intrinsic (green box) and extrinsic (yellow box) partial dislocations.

In this article we are concerned with movement of 3ML defects in semiconductor NWs. Like a dissociated crystal dislocation, the attractive forces between the constituent partials prevents their independent movement. However, unlike a dislocation, their long-range strain field strain fields cancel and to first order a 3ML defect is neither affected by stress fields nor generates surface image forces. Nevertheless, both partials can move conservatively, i.e. glide, on the (111) plane. Dislocation glide in semiconductors is commonly understood to be limited by the Peierls mechanism, i.e. to take place by movement of thermally-generated kinks along the core, each of which displaces the defect by one lattice translation vector on its glide plane.[18] For a kink to move one lattice translation along a partial dislocation in the zinc-blende structure, a single atomic bond must be broken and reformed and the energy barrier for this to take place determines the activation energy for dislocation movement.

Here, we consider the forces acting on 3ML defects and evaluate the efficacy of annealing to remove them from NWs, using atomic resolution scanning transmission electron microscopy (STEM) to image them in-

situ whilst heating up to 700 °C. We demonstrate that despite their lack of long-range strain field, the majority of null Burgers vector line defects are not thermodynamically stable in a NW. We extract an upper limit to the activation energy of approx. 2eV for the movement of 3ML defects – as expected, this is similar to that for dislocation glide. We find that certain configurations can be removed via post-growth annealing, but some null Burgers vector defects are stable and remain when the forces acting become very low. This strategy could be employed immediately after droplet consumption to improve material quality with little effort.

2. Theory

Line defects such as dislocations and 3ML defects increase the Gibbs free energy of a NW. The increase in energy depends on parameters such as the length of the defect and, for dislocations, the strain field induced in the crystal, which are a function of the location of the defect. If, by moving, the defect lowers the Gibbs free energy, an energy gradient is present, which is considered to be a force acting on the line defect. For example, when a 3ML defect terminates an enclosed twin such as that shown in Figure 1b, its lateral movement destroys, or creates, two {111} twin boundaries simultaneously. Each twin boundary has a significant energy per unit area, γ_{111}; there is therefore a force acting on the 3ML defect to reduce the area of {111} twin boundary in the NW. However, the force acting on any given defect depends upon its exact configuration, and we now consider this in more detail. The different configurations for 3ML defects in hexagonal {111} NWs are shown in Figure 2.

A second force may act on 3ML defects in addition to that resulting from changes in {111} twin boundary area, caused by a change of the defect length in a finite crystal. When a 3ML defect lies near the edge of the NW, its movement changes the length of {211} facet (configurations 1 and 2 in Figure 2a,). If, however, the surfaces where the 3ML defect emerges are parallel, (configuration 3 in Figure 2a), movement leaves its length unchanged and there is no additional force. Similarly, when a 3ML defect is an interfacial step (Figure 2b, top), lateral movement creates new twin boundary on one side while destroying it on the other

and, if the length of the defect does not change, there is no force acting on the defect. In this case, the defect is stable and will not move.

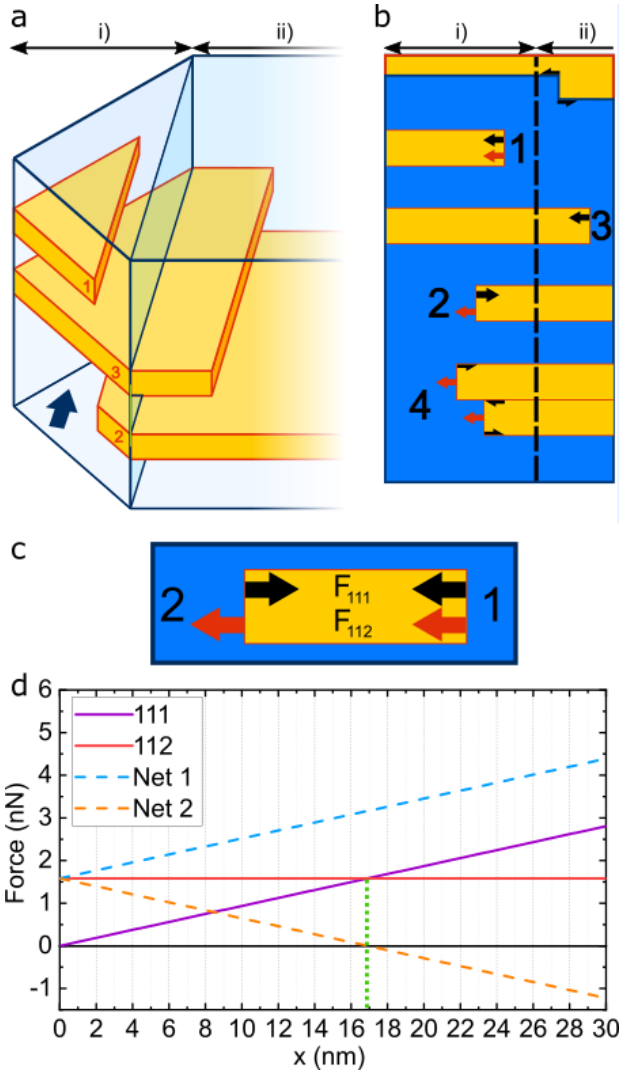

Figure 2 a) Different configurations of 3ML-thick twins in a NW. The short arrow indicates the [110] direction. b) The appearance of the different configurations in a), when viewed along [110]. The vertical dashed line indicates the boundary between regions (i) and (ii), with a tapering thickness and parallel sides, respectively. c) A combination of configurations 1 and 2 with forces acting on the 3ML defects. d) The forces acting on the different 3ML defects in c). The dashed green line shows where forces balance with a net force 0.

For clarity, we divide the nanowire into two regions, (i) where the thickness varies and (ii) with constant thickness, as shown in Figure 2a. The view along [110], used below in our high resolution STEM imaging, is shown in Figure 2b. We denote the energy per unit area of the {112} step facet and {111} twin boundary to be γ_{112} and γ_{111} respectively. For any given 3ML defect, the force acting upon it will depend upon the change in area of these twin boundaries. For example, in configuration (1) (Figures 2a, b, and the right of Figure 2c), movement of the 3ML defect to the left destroys upper and lower {111} twin boundaries and the {211} facet length also shrinks. Taking the x-direction to be to the right, a small movement $-\delta x$ of the 3ML defect, with length L and height H, gives a reduction in energy

$$\delta E_{(1)} = \gamma_{112} H \delta L + 2\gamma_{111} \delta A, \tag{1}$$

where A is the area of each {111} twin boundary. For the geometry shown in Figure 2, the changes in length and area are

$$\delta L = -\frac{2}{\sqrt{3}}\delta x \text{ and } \delta A = -L\delta x; \tag{2}$$

i.e. the force for configuration (1) is

$$F_{(1)} = \frac{\delta E}{\delta x} = F_{112} + F_{111} = -\frac{2}{\sqrt{3}}\gamma_{112} H - 2\gamma_{111} L, \tag{3}$$

where the negative sign indicates a force to the left for both terms. Interestingly, since the height of the defect does not change, F_{112} is independent of position. In contrast, F_{111} depends upon the length of the defect and decreases to zero when the 3ML defect reaches the edge of the NW. For configuration (2), i.e.

the 3ML defect on the left of Figure 2c, movement along $+x$ increases its length but decreases the {111} twin boundary area; the forces act in opposition to give

$$F_{(2)} = -\frac{2}{\sqrt{3}}\gamma_{112}H + 2\gamma_{111}L. \quad (4)$$

Finally, since the length of the 3ML defect is unchanged in configuration (3) it experiences a force

$$F_{(3)} = 2\gamma_{111}L \quad (5)$$

that is independent of position unless it leaves region (ii). We also show a fourth configuration in Figure 2c, a 6ML-high twin terminated by two 3ML defects. In addition to the net forces produced according to Equation (4), the energy is clearly lowered by elimination of the central {111} twin boundary, i.e. there is an attractive force between the two 3ML defects

$$F_{(4)} = \gamma_{111}L \quad (6)$$

The energy per unit area of a {111} ortho twin boundary is commonly estimated as half that of an intrinsic $1/6\langle 112\rangle$ stacking fault,[19] i.e. $\gamma_{111} \approx 27$ mJ m^{-2} in GaAs.[20] The force that is produced by a stacking fault on a partial dislocation is significant; in GaAs the repulsive force between two partials in a dissociated crystal dislocation is balanced by the stacking fault energy at a separation of only 4.1 nm.[21] Put another way, the force exerted on a 3ML defect by a twin boundary is roughly equivalent to that acting on a partial dislocation due to a shear stress of 1.2GPa, or a strained epitaxial layer with misfit of 0.5%.[see footnote 1] The disruption to tetrahedral bonding in the {112} para twin boundary means that γ_{112} is much larger; from density functional theory modelling, we estimate $\gamma_{112} \approx 980$ mJ m^{-2}.[13] Nevertheless, in a thick NW $L \gg H$ and the {111} term in Equations (4) and (5) may be expected to dominate, while closer to the thin edge of region (i) the opposite is true. The varying forces on 3ML defects as a function of position are shown in Figure 2d. Clearly, $|F_{(1)}| > |F_{(2)}|$ since the forces act in concert for the former, and in opposition for the latter. Since the length of the 3ML defect changes as a function of position, $F_{(2)}$ must become zero at some point, which we estimate to be approx. 15nm from the edge of the NW using the above values for γ_{111} and

γ_{112} (Figure 2d). The 3ML defect is stable in this position. In the case of twin segments thicker than 3ML (configuration (4) in Figure 2) the {112} term is larger, which shifts the point of stability deeper into the NW.

The above arguments show that most step facets are only thermodynamically stable under limited circumstances in a NW. In order to understand why we observe them we therefore need to consider their mechanism of movement. The well-established Peierls model of dislocations[18] may be used for 3ML defects if we consider them to be comprised of an intrinsic-extrinsic pair of $1/6\langle 112\rangle$ partial dislocations with opposite Burgers vectors, as shown in Figure 1. In bulk materials, dislocation motion is controlled by the nucleation rate of kink-pairs and diffusion of the kinks along the core.[18] For long dislocations, the velocity is controlled by the kink-pair rate per unit length of dislocation; kinks travel along the dislocation until they collide with a kink of opposite sign and annihilate. For short dislocations, such as those comprising the 3ML defects in our NWs, kinks are more likely to reach the NW surface before meeting a kink of opposite sign. In this case, the probability of kink-pair nucleation – and hence velocity v – is proportional to the length of the defect. Observations of dislocation glide in strained layers show a clear linear dependence of velocity on thickness.[22] We may thus expect the velocity of a 3ML defect in a NW to be described by the relation[23]

$$v = cLF \exp\left(-\frac{Q}{k_B T}\right) = v_0(x) \exp\left(-\frac{Q}{k_B T}\right) \quad (7)$$

where c is a constant and Q is some average of the activation energies for kink-pair formation and diffusion along both constituent $1/6\langle 112\rangle$ partial dislocations. The second part of Equation (7) combines these different factors into a single prefactor v_0, which is a function of position x in the NW. Equations (3) to (6) show that the force F depends at least in part on the defect length L for all configurations. Thus, if motion is limited by double-kink nucleation the 3ML defect v_0 should therefore vary in proportion with L^2 and dramatic slowing of a 3ML defect as it approaches the edge of the NW might be might expected. However, single kink nucleation where the defect reaches NW surface may also occur, which would give

v_0 proportional to L. In any case, movement of a 3ML defect in a NW may be expected to vary considerably depending upon its exact location in a NW of varying thickness. As for the dependence of velocity on the height of the {211} twin facet, a 3ML defect requires coordinated movement of both its constituent partial dislocations, while a 6ML defect requires coordinated movement of four partial dislocations, and so on. Velocities should therefore decrease rapidly with increasing height of the {211} facet. The activation energy of these defects Q should be similar to that of a dissociated crystal dislocation, which is also comprised of partial dislocations. A typical estimate of activation energy for a 1/2<110> edge dislocation glide in GaAs is 1.3eV.[24,25]

In summary for this section, we expect most null Burgers vector defects to be unstable in a NW, but to have kinetically-limited (thermally-activated) motion that means they will not move out of a NW without a high temperature anneal. We expect different behavior during an anneal, depending upon the defect configuration, but in general they should shrink in size until they disappear. Larger twin facets should move more slowly. Nevertheless, when many defects coexist, configurations are likely to arise which prevent the straightforward movements shown in Figure 2; defects may remain stable, locked in place. In the following section we use in-situ heating TEM experiments to investigate the behavior of these defects at high spatial resolution and different temperatures. The real-time observations of different defects place an upper bound on the activation energy and comparison of their actual behavior with that expected from the above considerations.

3. Method

Self-catalyzed GaAsP nanowires were grown directly on (111) *p*-type Si substrates by solid-source molecular beam epitaxy (MBE) with an average tip composition of $GaAs_{0.9}P_{0.1}$. Detailed information can be found in Sanchez (2018).[14] The majority of NWs have regular hexagonal prism shapes as shown Supporting Figure S2. NWs were dispersed onto a DENS solutions heating chip with perforated Si_3N_4 membranes. We carried out heating experiments in a doubly-corrected ARM200F STEM operating at 200

kV with a fine-imaging probe, (beam current of approximately 23 pA) and a convergence semi-angle of ~25 mrad. We used a programmed sequence of gradually increasing temperatures, starting at 600 °C. For large temperature changes the response time of the heating chip is a few seconds. After each heating cycle the sample was cooled immediately to 400 °C to allow examination of several different sites. The motion of over 80 defects was measured across 3 different NWs for seven temperature cycles and one of these NWs was observed for a further five heating cycles. During heating and cooling the sample was observed continuously at low magnification, typically with an image size of 512x512 pixels and a dwell time of 10 μs/pixel (i.e. 2.6s per image). Table I summarizes the temperatures and times used. A small amount of decomposition of the NW surface was observed at the highest temperatures, as might be expected due to loss of group V elements. This did not appear to have any significant effect on defect behavior.

Cycle No.	**Temperature (°C) (±1°C)**	**Time (s)**	**Running Total Time (s)**
1	600	30	30
2	620	30	60
3	620	30	90
4	620	30	120
5	640	30	150
6	640	30	180
7	680	30	210
8	680	30	240
9	700	30	270
10	700	20	290
11	700	20	310
12	700	20	330
13	700	20	350

Table I. Temperatures and times used for in-situ STEM observation of defective GaAsP NWs.

4. Results & Discussion

Exposure of defective NWs to the temperatures given in Table I revealed three different behaviors for 3ML defects: a) complete removal from the NW; b) initial movement, followed by a halt in a stable configuration (e.g. trapped by other defects); and c) no movement (i.e. already in a stable configuration). The behavior of all observed 3ML defects is summarized in Figure 3. Figure 3a shows the removal of defects for seven temperature cycles, while histograms of velocities are shown in Figure 3b. The inset in Figure 3b shows bright field (BF) images of the NW tips used in this study before any exposure to temperatures. In the first temperature cycle at 620 °C, the vast majority (82%) of 3ML defects do not move. However, at 640 °C, 60% of the defects become mobile and significant numbers of defects begin to recombine or reach the NW surface after cycle 4. After two cycles at 640 °C more than half of the initially mobile 3ML defects have been lost. Notably, while the number of immobile defects does not change after the second cycle at any temperature, an increase in temperature causes previously stationary defects to move. At the end of the experiment 65% of 3ML defects have been removed; however almost 15% of the remaining defects remain mobile, indicating that 70% of defects could be removed by a slightly longer anneal. At 620 °C the fastest-moving defect reaches a velocity of 0.68 nm s^{-1}, while at 640 °C some 3ML defects reach 0.76 nm s^{-1}. At higher temperatures still the maximum speed does not change significantly, but greater numbers of defects move at moderate speeds (0.2 – 0.3 nm s^{-1}). Separate charts for the 3 NWs examined in this study are shown in Supporting Figure S3, where the thinner, tapered shape of NW1 shows faster removal of defects. The lack of higher defect speeds at higher temperatures is simply because fast-moving defects reach either the NW surface or a stable configuration in the first few temperature cycles. The wide range of velocities indicates the variety of forces that 3ML defects experience, which is consistent with the calculations of section 3. The relatively low velocities (dislocations in bulk GaAs experiencing similar forces reach velocities of several thousand nm s^{-1} [23] are consistent with the kink nucleation model and the low velocities

observed for defects in thin films.[22] The defects that do not move at all during annealing seem to be completely stable. (e.g. 3ML steps in the center of the NW, as shown at the top of Figure 2b and Supporting Figure S4, or 3ML with height greater than 1 3ML, configuration 4 in Figure 2b and Supporting Figure S4).

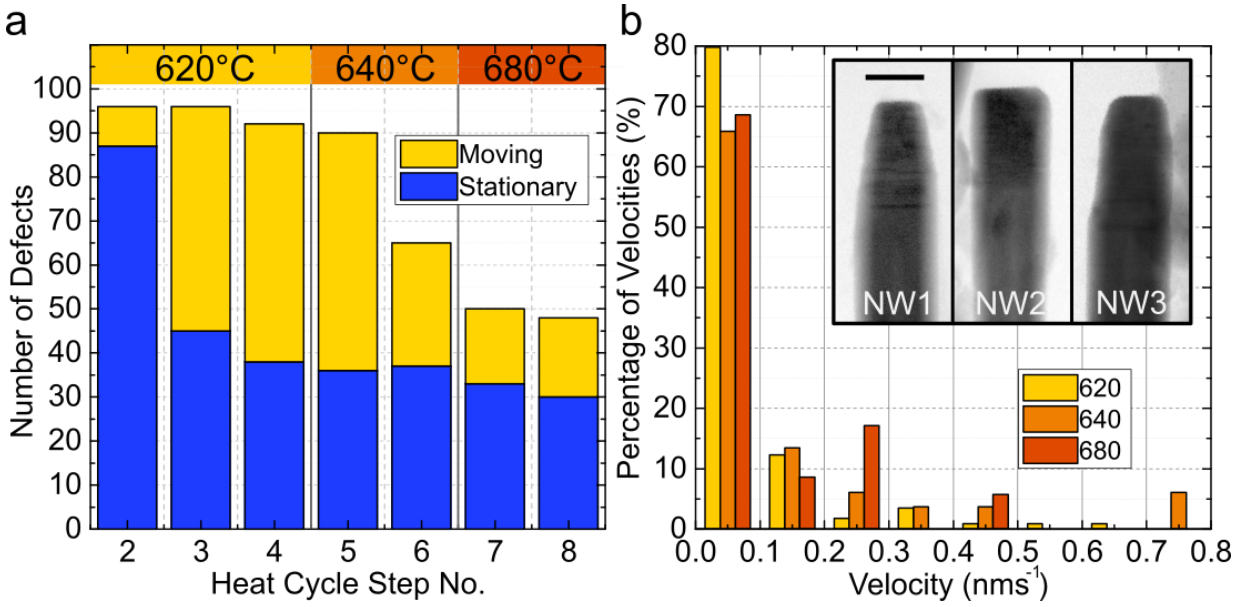

Figure 3. a) Number of defects observed (blue = stationary, yellow = mobile) and b) Histograms of defect velocities normalized to total number of velocities measured for each temperature observed during the temperature cycles given up to cycle number 8 in Table I. Inset shows BF-STEM images of the 3 NWs used in this study, scale bar is 100nm.

An example of the differing behavior of different 3ML defects, and the complete removal of a defect, is shown in Figure 4. This shows two 3ML defects at opposite ends of a twinned region approx. 15nm wide. The outside edge of the NW is to the left of the image, i.e. material thickness increases to the right. During heating the 3ML defect on the left is essentially stationary, while that on the right moves to meet it. The atom columns in the twinned region become blurred or indistinct during the period that the right-hand defect moves, indicating that the twin no longer occupies the full thickness of the NW along the electron beam direction. Although this blurring makes it difficult to observe the motion of the 3ML defect clearly, there

is no indication that it splits into its constituent $1/6\langle 112\rangle$ partials while moving. The different movements of the two 3ML defects is consistent with the calculations in section 2; the defect on the left is a type 2 configuration with forces that act in opposition, cancelling out, while that on the right starts as a type 3. Supporting Figure S6 shows how the intensity profile of an ADF image can be used to determine where the NW width becomes constant. Current defect on the left is approx. 36 nm from the edge of the NW, as shown in Supporting Figure S2. An example STEM video from a different NW showing motion of a similar configuration of defects is shown in Supporting Movie 2. The conditions used to obtain the video, along with an image of the same area before heating, the first movie frame and the final movie frame are provided in Supporting Information Figures S7a-c.

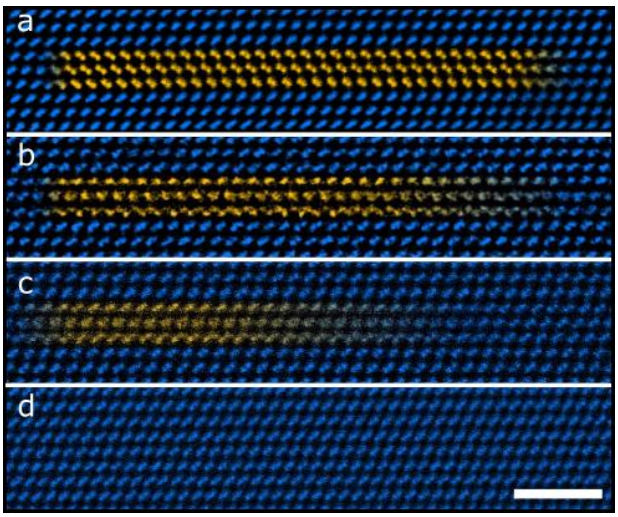

Figure 4. ADF-STEM images of 3ML defects in a type 1 configuration (right) and type 2 configuration (left), during exposure to the increasing temperatures given in Table I. a) before heating b) after step 7 c) step 8 d) step 9, at which point the twin has been completely removed from the nanowire. Scale bar is 2 nm.

Our observations of 3ML defect movement are limited by the time and temperature regimes that we can access inside the microscope. Since many defects have only a short distance to travel before reaching the

surface, only a few measurements are possible. Furthermore, extraction of an activation energy from the data is difficult due to the changing forces that 3ML defects experience as they move through the NW. Nevertheless, individual defects close to the axis of the NW that travel a long distance exhibit a clear increase in velocity at higher temperature as shown in Figure 5. Due to the hexagonal shape of the NW this region has a uniform thickness, meaning that the prefactor v_0 in Equation (7) should be constant. Figure 5a shows the area before any heating is applied. At the top configuration 3 is seen, with a 3ML twin that extends across most of the image, with a second 3ML step increasing the twin to a height of 6ML on the right. Another pair of 3ML defects that together make a 6ML-high twin can be seen at the bottom left of the image. A 4ML-high twin extends across the full width of the NW in the center. 5b-d shows this area after heating steps (6, 7 and 8). More heating steps are shown in Supporting Figure S8. The lower pair of 3ML defects quickly form a stationary 6ML defect. The upper 3ML defect becomes blurred and moves to the right, reducing the twin boundary area. The 3ML step at the top right hardly moves (as may be expected, since it makes no change in twin boundary area by doing so). When the two 3ML steps meet and form a 6ML facet, the motion stops, consistent with a low mobility of higher {211} facets. A plot of position for the upper 3ML defect at each temperature cycle shows a clear increase in velocity at higher temperatures (Figure 5e). A fit to the linear form of Equation 7 (Figure 5f) gives v_0 = 4 x 10^5 ms^{-1} and Q = 2.9 ± 0.6 eV, which was typical of type 3 configurations. Activation energies extracted in this way from all the data, including those close to the edges of the NW, varied considerably and gave values from 1.8 eV to 7.6 eV. These unreliable values simply show that the forces acting on the 3ML defects vary strongly with their position and a correct calculation requires a detailed knowledge of the exact shape of the NW. In addition to uncertainties about NW shape there are a formidable number of complicating factors that make quantitative study difficult. These include: the different core structure of up- and down-steps; the variation of stacking fault energy with temperature;[26] pinning by impurity segregation;[23,25,27] varying composition in a core-shell structure; changes to the NW surface during heating[28] and indeed the effect of the electron beam.[29–31] In the absence of this information, one can only say that these measurements only give an upper bound to the activation energy of ~2 eV.

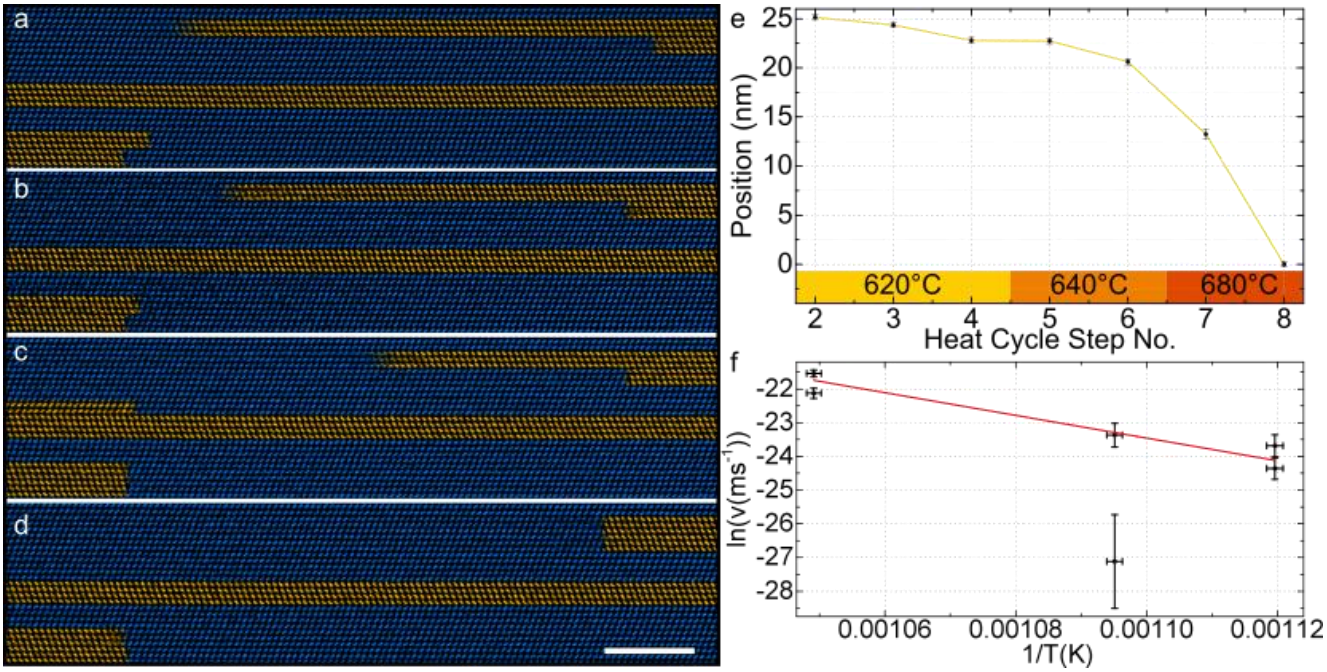

Figure 5. ADF-STEM images of 3ML defects close to the center of a GaAsP NW during exposure to the increasing temperatures given in Table I. a) before heating b) after step 6 c) step 7 d) step 8. Scale bar is 5 nm. e) The position of a 3ML defect relative to final defect position during the heating experiment. f) Measurement of the activation energy by fitting the data in (e) to the linear form of Equation (7). $Q = 2.9 \pm 0.6$ eV, ms^{-1}.

5. Summary and conclusions

In summary, we have shown that the majority of 3ML defects are unstable in a NW when exposed to high temperatures. Their movement is thermally activated, and they can be removed by post-growth annealing at temperatures above 640 °C. This is encouraging for the production of high-quality NWs for device applications, we find this method can remove more than 70% of defects in self-catalyzed NWs. The behavior of null Burgers vector defects is in many respects similar to that of partial dislocations and can be understood by considering the forces acting on them to reduce twin boundary area inside the NW. Nevertheless, roughly 25% of defects do not move at all in our experiments and are truly stable. An obvious

strategy to improve material quality is to employ an anneal immediately after droplet consumption and prior to growth of shell layers. Furthermore, the temperatures required may be significantly lower for pristine NWs in the growth chamber in comparison with the very rapid post-growth annealing of NWs employed here..

6. Associated Content

Supporting Information

Further TEM and ADF images of defect formation, defect motion and stable defects.

Supporting Movie 1: A TEM video of a NW with catalyst droplet still attached being heated in-situ and cooled and the formation of a defect observed.

Supporting Movie 2: An ADF STEM video of observed defect motion.

7. Author Information

Corresponding authors:

R.Beanland@warwick.ac.uk

A.M.Sanchez@warwick.ac.uk

ORCID:

J. A. Gott: 0000-0001-8521-5104

H. A. Fonseka: 0000-0003-3410-6981

A. M. Sanchez: 0000-0002-8230-6059

Y. Zhang: 0000-0002-2196-7291

8. Acknowledgements

This work was supported by EPSRC grants EP/P000916/1, EP/P000886/1 and EP/P031544/1. J.A.G. was supported by EPSRC EP/N509796/1. The authors would like to thank the Warwick Electron Microscopy RTP for technical support.

(1) Dasgupta, N. P.; Sun, J.; Liu, C.; Brittman, S.; Andrews, S. C.; Lim, J.; Gao, H.; Yan, R.; Yang, P. *Advanced Materials* **2014**, *26* (14), 2137–2184.
(2) Joyce, H. J.; Boland, J. L.; Davies, C. L.; Baig, S. A.; Johnston, M. B. *Semicond. Sci. Technol.* **2016**, *31* (10), 103003.
(3) Ma, R.-M.; Oulton, R. F. *Nature Nanotechnology* **2019**, *14* (1), 12.
(4) Zhang, Y.; Wu, J.; Aagesen, M.; Liu, H. *J. Phys. D: Appl. Phys.* **2015**, *48* (46), 463001.
(5) Yan, R.; Gargas, D.; Yang, P. *Nature Photonics* **2009**, *3* (10), 569–576.
(6) Eaton, S. W.; Fu, A.; Wong, A. B.; Ning, C.-Z.; Yang, P. *Nature Reviews Materials* **2016**, *1* (6), 16028.
(7) LaPierre, R. R.; Robson, M.; Azizur-Rahman, K. M.; Kuyanov, P. *J. Phys. D: Appl. Phys.* **2017**, *50* (12), 123001.
(8) Zhang, C.; Miao, X.; Chabak, K. D.; Li, X. *J. Phys. D: Appl. Phys.* **2017**, *50* (39), 393001.
(9) Royo, M.; Luca, M. D.; Rurali, R.; Zardo, I. A Review on III–*J. Phys. D: Appl. Phys.* **2017**, *50* (14), 143001.
(10) Jacobsson, D.; Panciera, F.; Tersoff, J.; Reuter, M. C.; Lehmann, S.; Hofmann, S.; Dick, K. A.; Ross, F. M. *Nature* **2016**, *531* (7594), 317–322.
(11) Heon Kim, Y.; Woo Park, D.; Jun Lee, S. *Appl. Phys. Lett.* **2012**, *100* (3), 033117.
(12) Dastjerdi, M. H. T.; Boulanger, J. P.; Kuyanov, P.; Aagesen, M.; LaPierre, R. R. *Nanotechnology* **2016**, *27* (47), 475403.
(13) Sanchez, A. M.; Zhang, Y.; Tait, E. W.; Hine, N. D. M.; Liu, H.; Beanland, R. *Nano Lett.* **2017**, *17* (4), 2454–2459.
(14) Sanchez, A. M.; Gott, J. A.; Fonseka, H. A.; Zhang, Y.; Liu, H.; Beanland, R. *Nano Lett.* **2018**, *18* (5), 3081–3087.
(15) Zamani, M.; Tütüncüoglu, G.; Martí-Sánchez, S.; Francaviglia, L.; Güniat, L.; Ghisalberti, L.; Potts, H.; Friedl, M.; Markov, E.; Kim, W.; Leran, J-B; Dubrovskii, V. G.; Arbiol, J; Morral, A. F. Nanoscale **2018**, 10 (36), 17080–17091.
(16) Xu, L.; Xu, D.; Tu, K. N.; Cai, Y.; Wang, N.; Dixit, P.; Pang, J. H. L.; Miao, J. *Journal of Applied Physics* **2008**, *104* (11), 113717.
(17) Cohen, D.; Carter, C. B. *Interface Science* **2003**, *11* (4), 391–401.
(18) Hirth, J. P.; Lothe, J. *Theory of Dislocations*; Kreiger Publishing Company, 1982.
(19) Glas, F.; Harmand, J.-C.; Patriarche, G. *Phys. Rev. Lett.* **2007**, *99* (14), 146101.
(20) Gottschalk, H.; Patzer, G.; Alexander, H. *physica status solidi (a)* **1978**, *45* (1), 207–217.
(21) Gottschalk, H. *J. Phys. Colloques* **1979**, *40* (C6), C6-127-C6-131.
(22) Maeda, K.; Yamashita, Y. *physica status solidi (a)* **1993**, *138* (2), 523–532.
(23) Sumino, K. Mechanical Behaviour of Semiconductors. In *Handbook on Semiconductors*; Elsevier Science: Amsterdam, 1994; Vol. 3a, pp 73–182.
(24) Jones, R.; Öberg, S.; Marklund, S. *Philosophical Magazine B* **1981**, *43* (5), 839–852.
(25) Yonenaga, I.; Sumino, K. *Journal of Applied Physics* **1989**, *65* (1), 85–92.
(26) Moon, W.-J.; Umeda, T.; Saka, H. *Philosophical Magazine Letters* **2003**, *83* (4), 233–247.
(27) Yonenaga, I.; Sumino, K. *Journal of Applied Physics* **1987**, *62* (4), 1212–1219.
(28) Chou, Y.-C.; Panciera, F.; Reuter, M. C.; Stach, E. A.; Ross, F. M. *Chem. Commun.* **2016**, *52* (33), 5686–5689.
(29) Chin, A. K.; Keramidas, V. G.; Johnston, W. D.; Mahajan, S.; Roccasecca. *Journal of Applied Physics* **1980**, *51* (2), 978–983.

(30) Maeda, K.; Yamashita, Y.; Maeda, N.; Takeuchi, S. *MRS Online Proceedings Library Archive* **1990**, *184*.
(31) Lavagne, S.; Levade, C.; Vanderschaeve, G, *Philosophical Magazine* **2006**, *86* (29–31), 4923–4940.

Footnote 1: stacking fault force acting on a partial dislocation

The attractive force per unit length between dissociated partial dislocations is

$$\frac{F}{L} = \frac{Gb^2}{4\pi d} \qquad \text{A1}$$

Where G is the shear modulus, (G_{GaAs} = 7.5x10^{10} Pa), b the Burgers vector magnitude of the dislocations (b = 2.31x10^{-10} m) and d is the spacing between them (d = 4.1x10^{-9} m)[19]. This gives F/L = 78 N mm^{-1}. The force per unit length on a partial dislocation in an epitaxial layer with strain of f is

$$\frac{F}{L} = \sigma_{ij} m_j b_i = \frac{2G(1+\nu)f}{\sqrt{3}(1+\nu)} \begin{bmatrix} 1 & 0 & 0 \\ 0 & 1 & 0 \\ 0 & 0 & 0 \end{bmatrix} \begin{bmatrix} 1 \\ 1 \\ 1 \end{bmatrix} \cdot \frac{a}{6} \begin{bmatrix} 2 \\ -1 \\ -1 \end{bmatrix} \qquad \text{A2}$$

where σ_{ij} is the stress tensor, m_j is the unit normal to the glide plane and b_i is the Burgers vector. Equating A1 and A2 gives $\sigma_{ij} m_j$ = 1.16x10^{9} Pa and f =0.5%.